

VISUALIZING NUCLEOSOME CLUSTER DYNAMICS WITH DIRECT STOCHASTIC
OPTICAL RECONSTRUCTION MICROSCOPY

PHD PRELIMINARY EXAMINATION

DEPARTMENT OF PHYSICS

BY

CLAYTON W. SEITZ

FALL 2023

TABLE OF CONTENTS

ABSTRACT	iii
0.1 Introduction	1
0.1.1 Visualizing nucleosome cluster dynamics in BRD4 condensates at super-resolution	1
0.1.2 Single molecule localization microscopy	2
0.2 Results	4
0.2.1 Dense two-dimensional and sparse three-dimensional SMLM	4
0.2.2 Visualizing nucleosome cluster dynamics in at super-resolution	6
0.2.3 Inhibition of a super-enhanced gene with JQ1	6
0.3 Future Aims	11
0.3.1 Specific Aim 1: Measure nucleosome cluster dynamics in living cells	11
0.3.2 Specific Aim 2: Determine effects of JQ1 and 1,6 Hexanediol exposure on nucleosome organization	12
0.4 Materials and Methods	13
0.4.1 Cell culture, transfection, and treatments	13
0.4.2 RNA fluorescence in-situ hybridization	13
0.4.3 Immunofluorescence	14
0.4.4 Quantitative reverse transcription polymerase chain reaction	14
0.4.5 Immunoblotting	15
0.4.6 Super-resolution imaging of nucleosome nanodomains	15
0.4.7 Sparse localization with maximum likelihood estimation	16
0.4.8 Dense localization with convolutional neural networks	18
0.4.9 Uncertainty quantification with Markov Chain Monte Carlo	19
0.4.10 Gaussian mixture model for correcting localization artifacts	19
0.5 Supplemental Information	20
0.5.1 Estimator precision sets the resolution limit in localization microscopy	20
0.5.2 Integrated isotropic and anisotropic Gaussian point spread functions	24
0.6 References	25

ABSTRACT

Single-molecule localization microscopy (SMLM) techniques, such as direct stochastic optical reconstruction microscopy (dSTORM), can be used to produce a pointillist representation of nucleosome organization at diffraction-unlimited precision. Direct STORM approaches leverage the deactivation of standard fluorescent tags, followed by spontaneous or photoinduced reactivation, which can be used to achieve super-resolution reconstructions of nuclear proteins and nucleic acids. This basic principle remains one of the method's primary limitations - standard SMLM fitting routines require tight control of activation and reactivation to maintain sparse emitters, presenting a tradeoff between imaging speed and labeling density. Here, we present a dSTORM strategy for fast reconstruction of nucleosome organization in living cells by complementing high duty-cycle blinking of rhodamine-derived dyes with a localization algorithm based on deep neural networks. Our strategy permits live cell imaging of nucleosome nanodomains, permitting physical analysis of their composition and evolution during biophysical processes such as phase separation. By performing high density localization and multi-color imaging, we intend to directly visualize nucleosome cluster dynamics and chromatin mobility following BRD4 inhibition with small molecule drugs JQ1 and 1,6 Hexanediol.

0.1 Introduction

0.1.1 *Visualizing nucleosome cluster dynamics in BRD4 condensates at super-resolution*

The nucleosome is the fundamental structural unit of DNA packaging in eukaryotic cells. It consists of approximately 146 base pairs (bp) of DNA wrapped in 1.67 left-handed superhelical turns around a histone octamer, consisting of 2 copies each of the core histones H2A, H2B, H3, and H4. (Luger 1997). Super-resolved nucleosome organization has been studied extensively in various epigenomic states to reveal segregated nanoclusters, dispersed nanodomains, and compact large aggregates. Nucleosomes assemble into heterogeneous clusters of variable sizes, interspersed with nucleosome-depleted regions (Ricci 2015). Histones can be decorated with various post-translational modifications such as acetylation, methylation, phosphorylation, and ubiquination. The recruitment of proteins and complexes with specific enzymatic activities is now a well-accepted dogma of how modifications mediate their function. Histone modifications can influence transcription of genes, and many other DNA processes such as repair, replication and recombination (Bannister and Kouzarides, 2011).

Here, we study live-cell dynamics of nucleosome organization, with a particular focus on the structure of biomolecular condensates containing bromodomain protein 4 (BRD4) protein, a major tandem-bromodomain-containing transcriptional regulator. BRD4 plays an important role in diverse cellular functions such as transcription, replication, epigenetic regulation, and DNA repair, and has been implicated in cancer and autoimmune diseases. BRD4 acetylates Lysine 122 on H3 (H3K122), a residue critical for nucleosome stability, resulting in nucleosome eviction and chromatin decompaction (Devaiah 2016). The intrinsically disordered regions (IDRs) of BRD4 are thought to facilitate its phase separation with coactivators such as MED1. The phase separation properties of BRD4 have been well-studied in several cell lines (Han 2020), and in the context of super-enhancers (Sabari 2018).

Selection bromodomain inhibitors, such as JQ1 are often employed to displace BRD4 protein from chromatin (Filippakopoulos 2010). 1,6-hexanediol (1,6-HD), an aliphatic alcohol, can inhibit weak hydrophobic protein-protein interactions required for the droplet formation (droplet melting activity) and is widely used to elucidate the formation process of nuclear bodies (Duster 2021). However, the effects of BRD4, and phase separation at large, on the spatial structure of nucleosome nanodomains remains unclear. We envision a complementary approach, consisting of specific and non-specific inhibition of BRD4-containing condensates in fixed cell ensembles and fast inhibition of phase separation in living cells with 1,6 Hexane-diol. Previous approaches to studying the dynamics of chromatin nanodomains only provide ensemble snapshots of chromatin structure, possibly due to slow acquisition times (Nozaki 2017).

0.1.2 Single molecule localization microscopy

Single molecule localization microscopy (SMLM) relies on the temporal resolution of fluorophores in the sample whose spatially overlapping point spread functions would otherwise render them unresolvable at the detector. SMLM techniques, such as stochastic optical reconstruction microscopy (STORM) and photo-activated localization microscopy (PALM) remain desirable for super-resolution imaging of many cellular structures, due to their cost-effective implementation and photon-count limited resolution (Schermelleh 2019). Common strategies for the temporal separation of molecules involve transient intramolecular rearrangements to switch from dark to fluorescent states or the exploitation of non-emitting molecular radicals. For direct STORM, rhodamine derivatives can undergo intersystem crossing to a triplet state, which can be reduced by thiols to form a dark radical species. The dark state can then be quenched by oxidative processes, driving the fluorophore back to its ground state (Figure 1). Long dark state lifetimes are commonly used in STORM imaging, while quenching results in higher duty cycle photoswitching and increased rates of

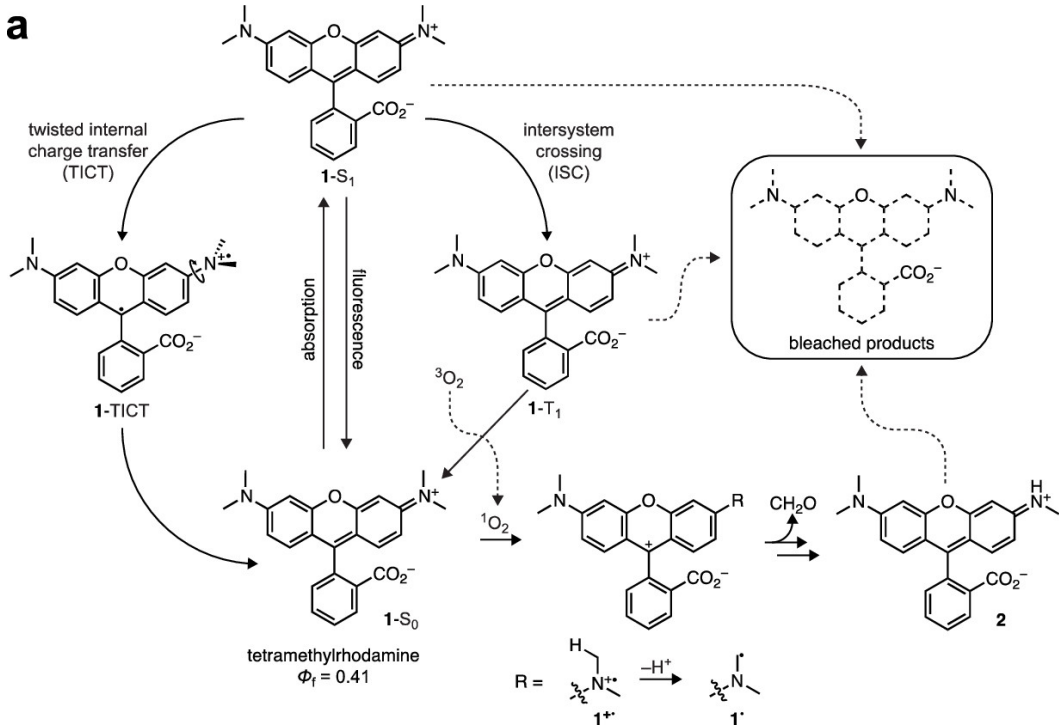


Figure 1: Photophysics of tetramethylrhodamine (TMR) and its derivatives JF549 and JF646. Maximum absorption occurs at 549nm or 646nm respectively and return to the ground state can occur via twisted internal charge transfer or inter-system crossing (Grimm 2021).

photobleaching due to irreversible oxidative damage of important functional groups. Long dark state lifetimes are frequently achieved by using an oxygen scavenging buffer containing glucose oxidase, catalase, and others.

Fluorescent labeling density has been known to pose a major bottleneck to super-resolution imaging acquisitions. Static uncertainty due to molecular crowding can be partially ameliorated by using pairwise or higher-order temporal correlations within a pixel neighborhood, known as stochastic optical fluctuation imaging (Dertinger 2009). Other approaches such as stimulated emission and depletion (STED) imaging bring control over the photophysical state of a chosen subset of the sample, yet the need for laser scanning prevents widespread application in live-cell studies. Furthermore, the spatial resolution and relative simplicity of SMLM techniques remains unmatched, inciting an effort to increase the time resolution

of STORM and PALM methods. The resolution of SMLM methods is limited only by the variance of a statistical estimator of molecular coordinates (Chao 2016). When we refer to localization error or uncertainty in this work, we are referring to aleatoric or systematic uncertainty, due to imperfections gradient-based estimators or convolutional networks. The posterior distribution on molecular coordinates can be computed using Markov Chain Monte Carlo techniques, but this is used sparingly for particle filtering, due to limited computational resources (Figure 7). Interestingly, recent work on integration of Bayesian priors with modulation enhanced SMLM (meSMLM) has generalized localization microscopy to a Bayesian setting, reducing spatial resolution below 1 nanometer (Kalisvaart 2022). In the time domain, previous approaches to improving resolution in SMLM fall into two main categories: generative models and dense localization methods. Generative methods learn prior information about cellular structures from super-resolution images, which is used to predict super-resolution images based on sparse localizations or widefield images (Ouyang 2018; Barth 2020; Chen 2023). Other approaches use convolutional neural networks to interpolate and transform dense images into a localization map (Nehme 2020; Speiser 2021). Here, we adapt the latter methodology, as biological structures such as chromatin are dynamic and intrinsically heterogeneous; therefore, structures cannot necessarily be known apriori, and deep generative models can hallucinate image artifacts.

0.2 Results

0.2.1 Dense two-dimensional and sparse three-dimensional SMLM

Two major factors contribute to localization errors in SMLM: (i) the noise characteristics of CMOS cameras and (ii) crowding of molecules within a diffraction limited region. Maximum likelihood estimation is frequently used for isolated molecules and high signal levels, retaining localization errors from 30-40nm (Figure 3c). However, MLE performance tends

to degrade in low SNR and dense regimes ($K(\lambda/2NA) > 1$), requiring more sophisticated localization methods, such as convolutional neural networks (CNNs). We employ a convolutional neural network, which successively upsamples a monochrome image and outputs a localization map, which can be post-processed to produce molecular coordinates (Figure 2b). We demonstrate that this architecture can outperform maximum likelihood estimation for all signal levels and molecular densities tested (Figure 2c).

To generalize our imaging setup to three-dimensions, we could use that the lateral point spread function has a weak dependence on the axial coordinate (Figure 3a). However, it has been shown that the error around the focus can be large, while negative and positive defocus cannot be distinguished given the symmetric dependence in z (Holtzer 2007). Instead, we choose to introduce astigmatism into the detection path using a weak cylindrical lens (Figure 4a). In effect, this breaks the axial symmetry of the PSF and gives an anisotropic Gaussian which is elongated perpendicular to the optical axis. Localization proceeds by measuring this anisotropy and inverting a model of its axial dependence. At high numerical aperture, a strong dependence of the anisotropy to axial displacement potentially provides more precise three-dimensional localization (Figure 4b). In general, the axial anisotropy can be complex, but is often well described by a polynomial function of the axial displacement (Smith 2010). Unfortunately, astigmatic imaging increases the width of the point spread function significantly, exacerbating localization errors by molecular crowding and low signal to noise ratio. Therefore, we report error statistics for maximum likelihood based methods only, and leave three-dimensional localization with CNNs to future work. As one might expect, at ideal SNR, we show that axial dependence of localization error bears a strong similarity to the axial dependence of the PSF width (Figure 4c). Lateral RMSE can be maintained below 40nm for the anisotropic PSF for $K(\lambda/2NA) \leq 5$; however, the Jaccard index tends to rapidly degrade at higher molecular densities, making MLE an unsuitable estimator for dense three-dimensional imaging (Figure 5). Three-dimensional single molecule

tracking with sparse emitters remains a good application of this method, and will be used in future work.

0.2.2 Visualizing nucleosome cluster dynamics in at super-resolution

Here, we use the HaloTag system, a modified haloalkane dehalogenase designed to covalently bind to synthetic ligands (Los 2008). The HaloTag protein is fused to H2B, either through transfection and clonal selection, or by transient transfection. The HaloTag is bound by a rhodamine-derived fluorescent ligands, JF549 or JF646, in order to (Grimm 2015). For super-resolution or three-dimensional single molecule tracking, we use oblique illumination microscopy to illuminate a thin area within a single nucleus (Tokunga 2008; Nozaki 2017).

0.2.3 Inhibition of a super-enhanced gene with JQ1

The guanylate binding protein (GBP) gene cluster codes for a family of interferon-gamma inducible GTPases. A recent study has confirmed phase separation in the GBP gene family region by co-staining of BRD4 and MED1 marker protein with the GBP gene family region, after infection of macrophages with *Mycobacterium tuberculosis* (Lin 2022). This result is a strong indication that the GBPs gene region tends to relocate into a phase-separated condensate containing BRD4 to efficiently initiate the immune response program. Leveraging previous work on the GBP gene cluster, we (i) confirm the efficacy of JQ1 treatment on GBP5 knockdown after interferon-gamma induction and (ii) determine the effects of JQ1 exposure on BRD4 immunofluorescence signal in Hela nuclei. Fluorescence in-situ hybridization (FISH) demonstrated the formation of GBP5 positive puncta in Hela nuclei after interferon-gamma exposure (Figure 5A-C,F) and mRNA expression over several hours (Figure 5D.) Relief of GBP5 expression was observed by incubating Hela cells for 8h with both interferon-gamma and JQ1 (Figure 5E). BRD4 puncta are abundant in Hela nuclei and exposure of JQ1 for 9h showed a reduction in puncta counts to approximately 70 percent

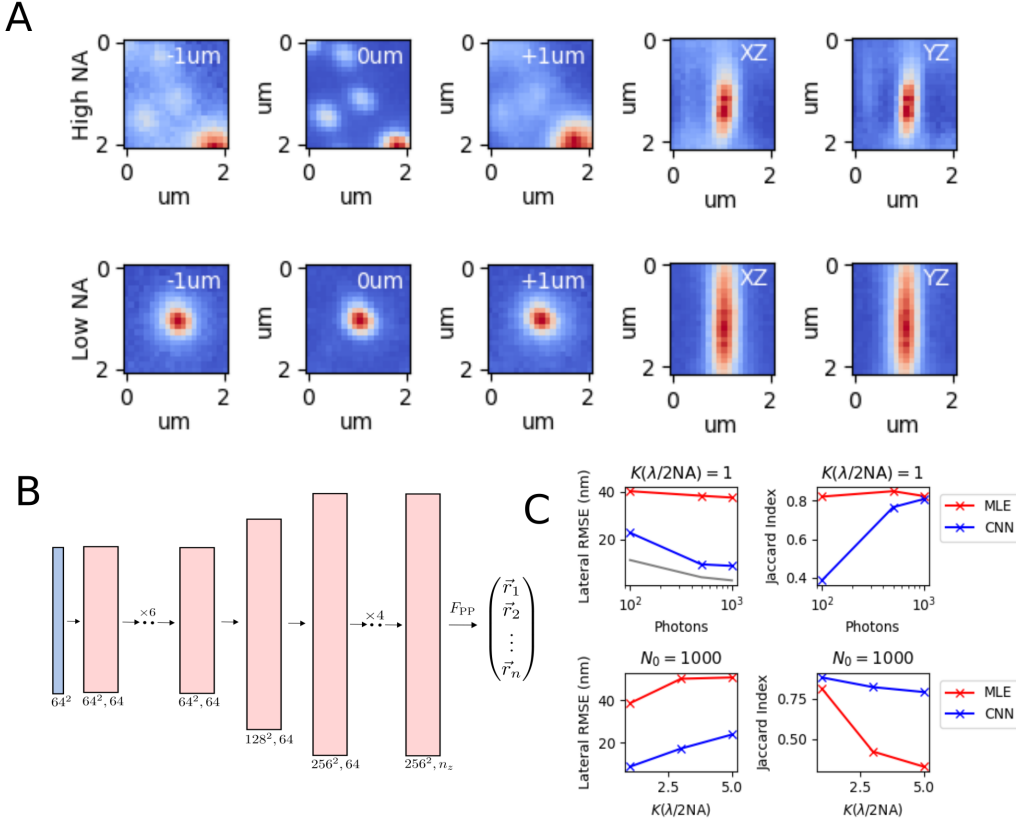


Figure 2: Convolutional neural networks outperform MLE in dense and low-signal cases (A) Lateral and axial point spread functions for high (~ 1.25) and low (~ 0.8) numerical aperture (NA). (B) Convolutional neural network architecture used for localization. A monochrome image is convolved and upsampled to generate a localization map, which is post-processed to produce a vector of coordinates. (C) Lateral root mean squared error of maximum likelihood estimator (MLE) and a convolutional neural network (CNN) with respect to the incident photon count and the number of molecules within the diffraction limit $\lambda/2NA$ for high NA. The Cramer-Rao lower bound on lateral uncertainty is shown in gray. Error samples = 10^3

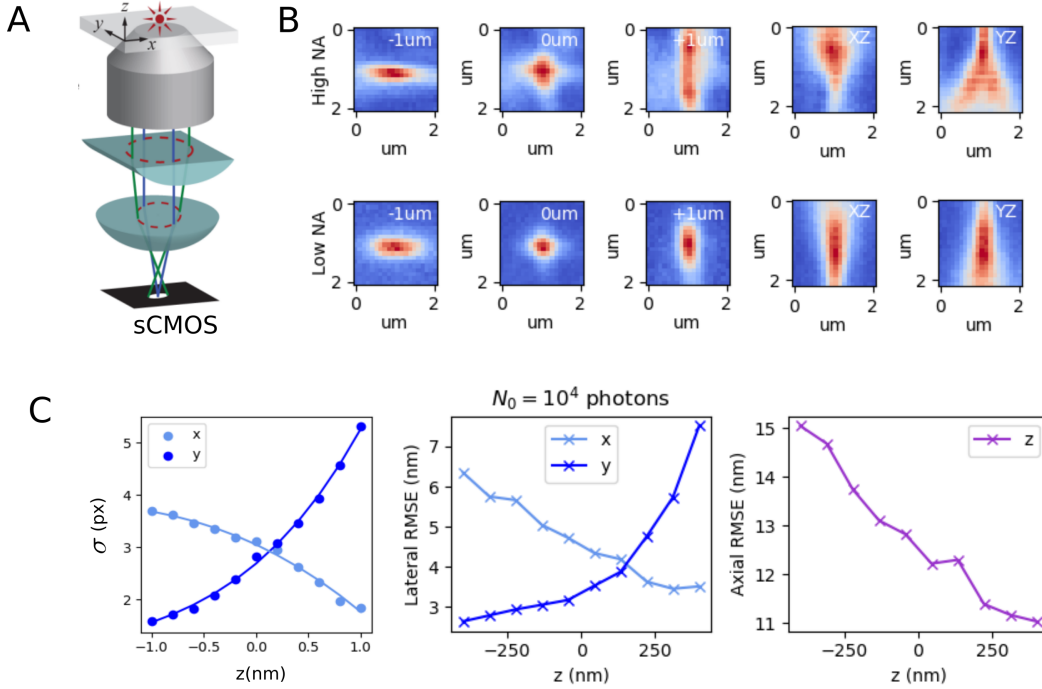


Figure 3: Axial precision for three-dimensional localization at ideal SNR

(A) Simplified lens relay for astigmatic imaging of a fluorescent emitter using a weak cylindrical lens ($f=10\text{m}$). (B) Lateral and axial point spread function of a single quantum dot on a 1.5 glass coverslip for high (~ 1.25) and low (~ 0.8) numerical aperture (NA). (C) Polynomial fit of the standard deviation of the lateral point spread function along orthogonal axes (left) Root mean squared error (RMSE) of lateral coordinates as a function of the axial coordinate, using simulated images fit with MLE (middle). RMSE of the axial coordinate, using simulated images fit with MLE (right). Error samples = 10^3

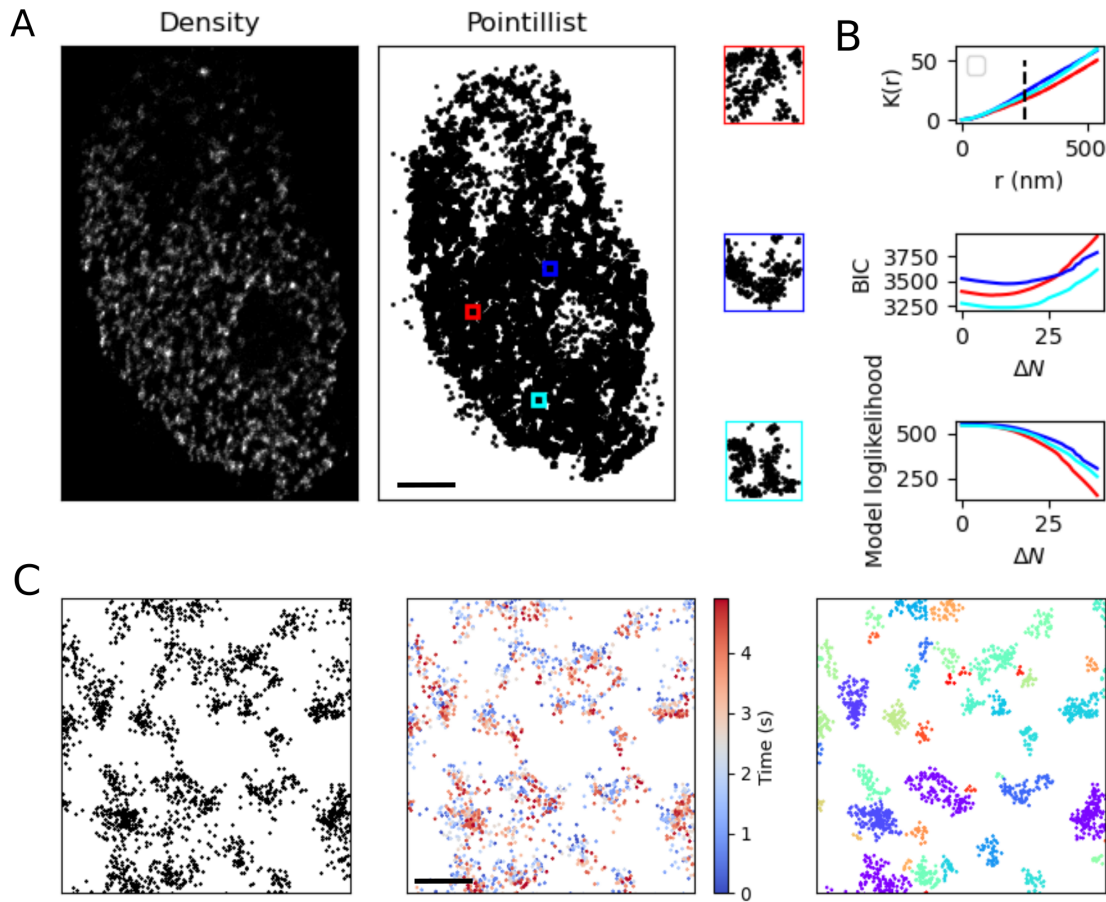


Figure 4: Super-resolution reconstruction of nucleosome organization in a living HeLa cell nucleus. (A) Density representation of nucleosome organization using 30nm x 30nm bins and a pointillist representation of nucleosome organization (B) Ripley's K function, Bayesian information criterion (BIC), and log likelihood for a Gaussian mixture model of pointillist localization data of three randomly selected regions of interest. Dashed line drawn at the diffraction limit (C) Localization accumulation over five seconds of imaging time (500 frames) and clustering with DBSCAN for a randomly selected region of interest

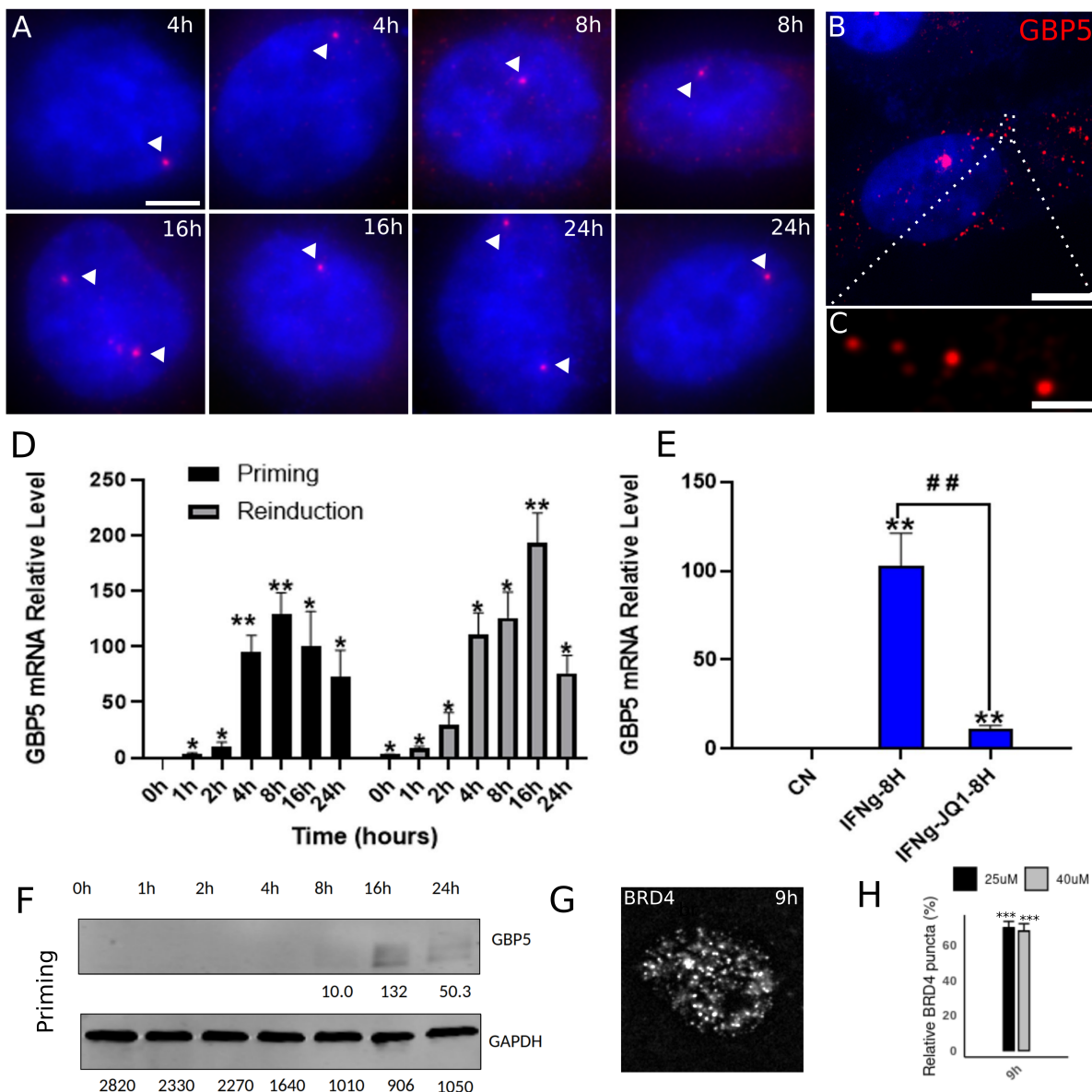


Figure 5: Inhibition of a super-enhanced gene with JQ1. (A) Putative GBP5 transcription sites at the specified time points following IFN- γ exposure. (B,C) High resolution zoom of GBP5 in-situ hybridization 8 hours following IFN- γ exposure (D) Induction of GBP5 expression in HeLa cells following IFN- γ exposure, measured with RT-qPCR (E) Knockdown of GBP5 expression 8 hours following IFN- γ exposure with 1 μ M JQ1 treatment ($n = 3, **P < 0.01$) (F) Western blot of GBP5 protein expression following IFN- γ exposure (G) BRD4 immunofluorescence 9h after first exposure to (+)JQ1 (H) Ratio of BRD4 puncta count 9h after JQ1 exposure relative to control ($n = 108, **P < 0.001$)

relative to control.

0.3 Future Aims

0.3.1 Specific Aim 1: Measure nucleosome cluster dynamics in living cells

Rationale and hypothesis

So far, super-resolved nucleosome clustering has been predominantly studied in fixed cells (Nozaki 2017; Itoh 2021). Live cell studies are limited by the low time resolution of SMLM and have so far relied on reconstruction of nucleosome reorganization by transforming wide-field images with convolutional neural networks. Using this technique, it has been reported that nucleosome clusters reorganize on millisecond to second time scales (Barth 2020). Therefore, we seek to apply our method to validate this result with fast two-color dSTORM microscopy on second time scales.

Experimental Approach

To perform this experiment, we have previously optimized simultaneous two-color labeling of H2B-HaloTag with JF549 and JF646. We maintain sparse labeling of H2B with JF549 using 10pM concentration and a short incubation time of 1 hour. The purpose of using JF549 is two fold: (i) Three-dimensional single molecule tracking can be performed on sparsely labeled samples with lower laser power than used in dSTORM (ii) Low laser power allows us to use this channel for autofocusing of the sample and performing cyclical imaging of the same living cell, with reduced photodamage. Moreover, we maintain dense labeling of H2B-HaloTag with JF646 for super-resolution imaging of nucleosome clusters. Experiments will be carried out on a live cell microscope based on an Olympus IX83.

0.3.2 Specific Aim 2: Determine effects of JQ1 and 1,6 Hexanediol exposure on nucleosome organization

Rationale and hypothesis

Our previous results have validated the efficacy of JQ1 in inhibiting the expression of BRD4-controlled gene GBP5. This result is consistent with previous colocalization studies of the GBP locus with MED1 and BRD4 and identification of the GBP super enhancer (Lin 2022). JQ1 is a cell permeable small molecule that binds competitively to the acetyl-lysine binding cavity of BRD4, displacing BRD4 from chromatin (Fillappakopoulos 2010). BRD4 is known to play a role in nucleosome eviction as well as phase separation in nuclear bodies; however, it remains unclear the primary effects of BRD4 on nucleosome organization. JQ1 does indeed inhibit an array of genes, including GBP5 (Hogg 2017), but has had only a small effect on overall BRD4 residency in C33A nuclei (Han 2020). Therefore, it appears that the epigenetic role of BRD4 is more nuanced. For example, super-enhancers are far more sensitive to drugs blocking the binding of BRD4 to acetylated chromatin (Chapuy 2013; Loven 2013; Hnisz 2017). We hypothesize that large BRD4 aggregates are more susceptible to JQ1, while small aggregates can be dissolved with phase separation inhibitors, but not BET inhibitors alone.

1,6 Hexanediol exposure can rapidly induce broad reorganization of chromatin, providing a useful control for directly observing nucleosome cluster dynamics in mammalian cells. Nevertheless, changes in chromatin architecture following non-specific drugs can be difficult to decouple from induced changes in chromatin structure itself. Previous studies have demonstrated in fixed cells that nucleosome clusters are rapidly immobilized and condensed after exposure to 1,6 Hexanediol (Itoh 2021). However, nucleosome organization is highly irregular, heterogeneous, and dynamic, making ensemble statistics inappropriate for making strong conclusions in fast perturbation experiments.

Experimental Approach

JQ1 is a relatively slow acting small molecule drug. Therefore, we propose fixed cell experiments to validate its effect on BRD4 residency in the nucleus 2h, 4h, and 8h after exposure to 20uM JQ1. In fixed cell ensembles, we will measure size distributions of BRD4 clusters in control versus JQ1 treated cells. Later, we will transiently transfect BRD4-GFP fusion protein into Hela cells followed by three-color live cell imaging of BRD4, H2B-JF549, and H2B-JF646 following initial exposure to 1-5 percent 1,6 Hexanediol. Cells will be exposed to Hexanediol on the microscope stage, followed by cyclic super-resolution imaging. This phase will be used to determine the effects of Hexanediol exposure on BRD4 residency in the nucleus and differential effects of Hexanediol on BRD4-positive and BRD4-negative chromatin nanodomains.

0.4 Materials and Methods

0.4.1 Cell culture, transfection, and treatments

Hela cells were cultured in DMEM supplemented with 10 percent fetal bovine serum (Gibco) at 37C, 5 percent CO₂ in a humidified incubator. For super-resolution experiments, cells were seeded in a 35mm FluoroDish (WPI), and transiently transfected with pBREBACK-H2BHalo plasmid (Addgene plasmid 91564) using Lipofectamine 3000 (ThermoFisher). For immune activation, cells were incubated with 50ng/ml Interferon-gamma (Gibco), diluted in fresh DMEM. BRD4 inhibition with JQ1 (Chemie Tek) was carried out using specified concentrations and incubation time in fresh DMEM.

0.4.2 RNA fluorescence *in-situ* hybridization

Cells were seeded in 8-well chamber slides with 1.5 glass coverslip bottom (Ibidi). GBP5 expression was induced with 50ng/ml Interferon-gamma, followed by fixation. Stellaris RNA

FISH Wash Buffer A (Biosearch Technologies, Inc., SMF-WA1-60), 10 percent Deionized Formamide (EMD Millipore, S4117) in RNase-free water (Life Technologies, AM9932) for 5 min at RT. Cells were hybridized with 90 percent Stellaris RNA FISH Hybridization Buffer (Biosearch Technologies, SMF-HB1-10), 10 percent Deionized Formamide, 12.5 μ M Stellaris RNA FISH probes designed to hybridize introns of the . Hybridization was performed in a humidified chamber at 37C. Cells were then washed with Wash Buffer A for 30 min at 37°C and nuclei were stained with 15ng/ml DAPI in Wash Buffer A for 5 min at RT. After one 5-min wash with Stellaris RNA FISH Wash Buffer B (Biosearch Technologies, SMF-WB1-20) at RT. Images were acquired as 10x10 grids on an ASI RAMM widefield microscope with 60X 1.4NA Nikon oil-immersion objective using Micromanager acquisition software and a Hammamatsu ORCA-Flash4.0v3 camera.

RNA FISH probes were designed and generated by Biosearch Technologies Stellaris RNA FISH to target exons of GBP5.

0.4.3 Immunofluorescence

Cells grown in chamber slides or 35mm dishes and permeabilized with 0.3 percent (v/v) Triton-X100 (Sigma-Aldrich) in PBS and blocked for 1h in 5 percent (w/v) nonfat dry milk at 4C. Cells were incubated overnight at 4C using primary antibody anti-BRD4 (Cell Signaling, clone E2A7X; 1:1000). Secondary antibodies for BRD4 (Cell Signaling Anti-Rabbit IgG-Alexa488, 1:1000).

0.4.4 Quantitative reverse transcription polymerase chain reaction

GBP5 induction was validated with RT-qPCR, using the TaqMan gene expression assay. Cell culture followed standard procedure, followed by homogenization with lysis buffer with 2-mercaptoethanol (Bio-Rad). Suspension was vortexed and transferred into a clean RNase-free tube. The homogenate was centrifuged at 12,000g for 2 minutes. RNA was purified

using PureLink RNA Mini Kit (Invitrogen) and stored on ice. Reverse transcription was carried out using the iScript Advanced cDNA Synthesis Kit (Bio-Rad). Taqman probes were designed against GAPDH and GBP5 genes, and RT-qPCR was run in a 96 well plate on a qPCR machine (Applied Biosystems). Relative RNA level of GBP5 to GAPDH were computed using the $\Delta\Delta C_t$ method (Schmittgen 2008).

0.4.5 Immunoblotting

Cells were washed and lysis buffer added (RIPA buffer: PMSF: protease inhibitor cocktail: orthovanadate=100:1:1:1). Cells were then scraped and sonicated for 15 seconds using an ultrasonic homogenizer. Lysate was centrifuged at high speed (13200r/min) for 10-15 minutes at 4C to pellet the cellular debris. Total protein concentration was determined by a BCA Protein Assay Kit (Pierce). For electrophoresis, protein samples were prepared according to a protein-loading ratio of 3:1. Sample was mixed and heated at 95°C for 5 min, followed by vortex and centrifuge. After running the gel, it was removed from the cassette and assembled inside the Trans-Blot Turbo Transfer System cassette. Transfer was run at 2.5A for 7min. Sample was then blocked using 5 percent skim milk blocking solution prepared with PBST. Primary GBP5 antibody was diluted with PBST (1:1000) and incubated at 4C overnight. The secondary antibody was diluted with PBST (1:2000) and placed on a rocker and incubate at RT for 45min. Western blots on PVDF membranes were scanned using the Odyssey fluorescence scanning system software.

0.4.6 Super-resolution imaging of nucleosome nanodomains

After transient transfection, H2B-Halotag Hela cells were incubated with JF646 HaloTag ligand overnight. Living Hela cells were imaged in a dSTORM photoswitching buffer containing 100mM MEA, 50 ug/ml Glucose Oxidase, and 3.4 mg/ml Catalase (Sigma). Buffer pH was adjusted to 8 using HCl. Movies were collected using a custom Olympus IX83 mi-

croscope body equipped with an Olympus 60X 1.25NA oil-immersion objective. Images were projected onto an ORCA-Fusion sCMOS camera (Hamamatsu). The microscope was controlled using Micromanager software. JF646 molecules were illuminated with a 640nm laser held at 20mW, as measured at the back focal plane of the objective. Frames were captured at 100fps. Registration of movies was performed with StackReg rigid body registration.

0.4.7 Sparse localization with maximum likelihood estimation

For each pixel, the number of photoelectrons S_k is multiplied by a gain factor g_k [ADU/e⁻], which generally must be measured during calibration. The readout noise per pixel ξ_k is Gaussian with some pixel-specific offset o_k (Figure 2a) and variance σ_k^2 (Figure 2b). Ultimately, we have a Poisson component of the noise, which scales with the signal level and a Gaussian component, which does not. Therefore, in a single exposure, we measure:

$$\vec{H} = \vec{S} + \vec{\xi} \quad (1)$$

What we are after is the joint distribution $P(\vec{H})$. Fundamental probability theory states that the distribution of H_k is the convolution of the distributions of S_k and ξ_k ,

$$P(H_k|\theta) = P(S_k) \circledast P(\xi_k) \quad (2)$$

$$= A \sum_{q=0}^{\infty} \frac{1}{q!} e^{-\mu_k} \mu_k^q \frac{1}{\sqrt{2\pi}\sigma_k} e^{-\frac{(H_k - g_k q - o_k)^2}{2\sigma_k^2}} \quad (3)$$

where $P(\xi_k) = \mathcal{N}(o_k, \sigma_k^2)$ and $P(S_k) = \text{Poisson}(g_k \mu_k)$, A is some normalization constant and \circledast represents convolution. In practice, this expression is difficult to work with, so we look for an approximation. We will use the Poisson-Normal approximation to simplify Eq (4)

$$\xi_k - o_k + \sigma_k^2 \sim \mathcal{N}(\sigma_k^2, \sigma_k^2) \approx \text{Poisson}(\sigma_k^2)$$

Since $H_k = S_k + \xi_k$, we transform $H'_k = H_k - o_k + \sigma_k^2$, which is distributed according to

$$H'_k \sim \text{Poisson}(\mu'_k)$$

where $\mu'_k = g_k \mu_k + \sigma_k^2$. This result can be seen from the fact the the convolution of two Poisson distributions is also Poisson. The quality of this approximation will degrade with decreasing signal level, since the Poisson distribution does not retain its Gaussian shape at low expected counts. Nevertheless, the quality of the approximation appears to increase exponentially with the expected count, as measured by the Komogorov distance between the convolution distribution (4) and its Poisson approximation (Figure 2c).

Localization microscopy supposes that molecules really do have an exact location in space. In practice, this is only an approximation since molecules can diffuse at physiological temperatures, and our exposure time would need to tend to zero for this to be exactly true. If we suppose that we can collect a sufficient amount of photons in a short enough time, such that a definite position exists, the following optimization problem is defined

$$\theta_{\text{MLE}} = \underset{\theta}{\operatorname{argmax}} \prod_k P(H_k | \theta) = \underset{\theta}{\operatorname{argmin}} - \sum_k \log P(H_k | \theta)$$

where θ_{MLE} represents the maximum likelihood coordinates of a fluorescent molecule. Maximum likelihood estimation (MLE) is a natural choice, since optimization of coordinates under a Poisson likelihood is tractable. Under the Poisson approximation, the model negative log-likelihood is

$$\ell(\vec{H}|\theta) = -\log \prod_k \frac{e^{-(\mu'_k)} (\mu'_k)^{n_k}}{n_k!} \quad (4)$$

$$= \sum_k \log n_k! + \mu'_k - n_k \log (\mu'_k) \quad (5)$$

First order derivatives of the above sum can often be computed analytically, depending on the spatial function μ . The Poisson approximation is also convenient for computing the Fisher information matrix for θ_{MLE} and thus the Cramer-Rao lower bound, which bounds the variance of a statistical estimator of θ_{MLE} , from below (Chao 2016). Fisher information (separable case):

$$I_{ij}(\theta) = \mathbb{E}_{\theta} \left(\frac{\partial \ell}{\partial \theta_i} \frac{\partial \ell}{\partial \theta_j} \right) \quad (6)$$

Let $\mu'_k = \mu_k + \sigma_k^2$. For an arbitrary parameter,

$$\frac{\partial \ell}{\partial \theta_i} = \frac{\partial}{\partial \theta_i} \sum_k x_k \log x_k + \mu'_k - x_k \log (\mu'_k)$$

$$= \sum_k \frac{\partial \mu'_k}{\partial \theta_i} \left(\frac{\mu'_k - x_k}{\mu'_k} \right)$$

$$I_{ij}(\theta) = \mathbb{E}_{\theta} \left(\sum_k \frac{\partial \mu'_k}{\partial \theta_i} \frac{\partial \mu'_k}{\partial \theta_j} \left(\frac{\mu'_k - x_k}{\mu'_k} \right)^2 \right) = \sum_k \frac{1}{\mu'_k} \frac{\partial \mu'_k}{\partial \theta_i} \frac{\partial \mu'_k}{\partial \theta_j}$$

0.4.8 Dense localization with convolutional neural networks

We employ a localization CNN architecture based on DeepSTORM3D which consists of three main modules. The first module consists of successive dilated convolutions, followed by an upsampling module to increase the lateral resolution by a factor of 4. The third and last module adds additional convolutional blocks to refine localization estimates. This ar-

chitecture can also be used for three-dimensional localization and thus the final output has n_z channels. The final output is followed by an element-wise HardTanh (Maas 2013). A post-processing function F_{PP} uses a user-defined threshold to produce a matrix of coordinates. We find the performance of this architecture on simulated images surpasses MLE, and approaches the Cramer-Rao lower bound at high signal levels, retaining a RMSE near 20nm for $K(\lambda/2\text{NA}) \leq 5$, at high signal levels (Figure 3c).

0.4.9 Uncertainty quantification with Markov Chain Monte Carlo

To filter out suspicious localizations, we used Metropolis-Hastings Markov Chain Monte Carlo (MCMC) to estimate the posterior marginals on coordinates. MCMC is asymptotically exact, which is not guaranteed by variational methods which may rely on a Laplace approximation around the MLE. Metropolis-Hastings is run for 3000 iterations, the first half is discarded as burn-in. A proposal $\theta' = \theta + \xi$ was generated with $\xi \sim \mathcal{N}(0, \sigma^2 I)$ where $\sigma^2 = 0.01$. The acceptance probability is

$$\alpha = e^{\beta(\ell(\theta) - \ell(\theta'))}$$

with $\beta = 5$ to achieve a target acceptance rate of 0.3. Localizations with uncertainty exceeding 50nm are removed from the dataset.

0.4.10 Gaussian mixture model for correcting localization artifacts

In high duty cycle SMLM, the sample molecule can be localized several times throughout an imaging acquisition. We take a probabilistic approach, motivated by Occam’s razor, assuming stationary conditions in the sample. The localization data is used to construct a Gaussian mixture model (Bishop 2006) with one Gaussian mode per localization, parameterized by posterior variances. These can be computed with MCMC, but for simplicity we replace

them by the expected variance Σ_0 . We then compute the distance matrix D_{ij} between all localizations and iteratively selects the nearest pair of coordinates and fuses them by replacement with their average position: $\mu_1, \mu_2 \rightarrow \mu = \frac{\mu_1 + \mu_2}{2}$ and covariance Σ_0 . After each fusion, we compute the Bayesian information criterion (BIC):

$$\text{BIC} = k \ln(n) - 2 \ln(\mathcal{L})$$

where n is the number of localizations, $k = 2n$ is the number of parameters in the GMM, and \mathcal{L} is the data likelihood. We compute the model log-likelihood

$$\ell(\theta|\mathbf{r}) = \sum_n \pi_n \mathcal{N}(\mathbf{r}_n, \Sigma_0)$$

Iteration then proceeds to minimize the BIC.

0.4.11 Fourier Ring Correlation

Following (Nieuwenhuizen 2013), a pair of subsets is drawn from the full list of localizations, and isotropic Gaussian kernel density estimation is performed. The Fourier Ring Correlation is calculated as a function of the ring radius q for two images f_1 and f_2

$$\text{FRC}(q) = \frac{\sum_{\vec{q} \in \text{circle}} \tilde{f}_1(\vec{q}) \tilde{f}_2(\vec{q})^*}{\sqrt{\sum_{\vec{q} \in \text{circle}} |\tilde{f}_1(\vec{q})|^2} \sqrt{\sum_{\vec{q} \in \text{circle}} |\tilde{f}_2(\vec{q})|^2}}$$

where \tilde{f}_1 is the discrete Fourier transform of f_1 .

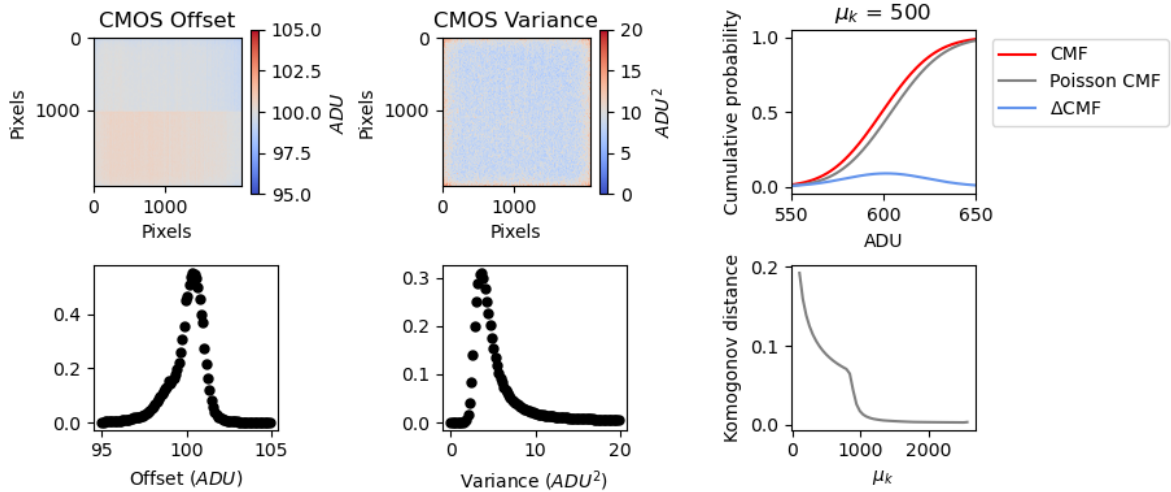


Figure 6: Noise characterization of Hamamatsu ORCA-Flash 4 CMOS sensor. (A) Offset for zero incident photons (B) Variance for zero incident photons (C) Cumulative mass function for the convolution distribution and its Poisson approximation for rate parameter $\mu_k = 500$ counts (D) Komogonov distance measured as a function of rate parameter μ_k

0.5 Supplemental Information

0.5.1 Estimator precision sets the resolution limit in localization microscopy

In recent years, Complementary Metal-Oxide-Semiconductor (CMOS) cameras have become a central tool in fluorescence microscopy. The CMOS sensor is revered for its high frame rates, allowing researchers to reach higher temporal resolutions. Nevertheless, CMOS cameras have noise sources intrinsic to their operation, such as shot noise and readout noise. The former phenomenon can describe a superposition of processes; namely, the fluctuations of the number of photons due to the quantum nature of light, and the random conversion of photons into photoelectrons within the semiconductor material with a quantum efficiency below unity. Here we will often refer to the photon count N_0 , which has a determined value, rather than being described by statistically. The *measured* photon count, however, is well-

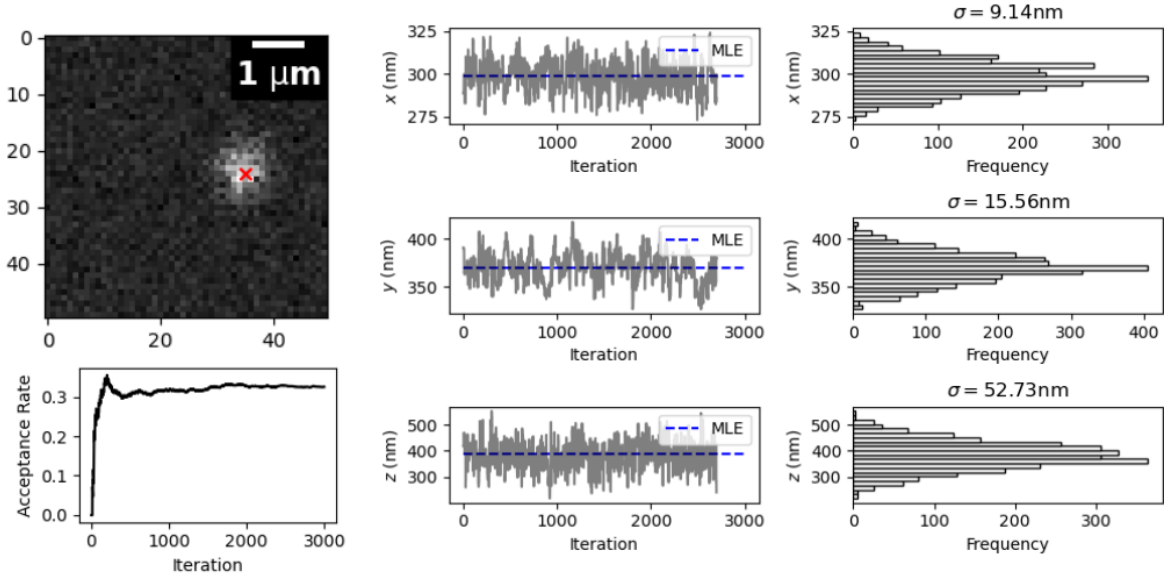


Figure 7: Computing epistemic uncertainties with Metropolis-Hastings. (top left) Simulated point spread function for $N_0 = 10^3$ photons with a red x at x_{MLE} and y_{MLE} (bottom left) Acceptance rate of Markov chain (middle) Markov chains sampling from the posterior distribution on molecule coordinates in 3D, with the maximum likelihood estimation in dashed blue (right) Estimated posterior marginals on the localization parameters with their respective uncertainties

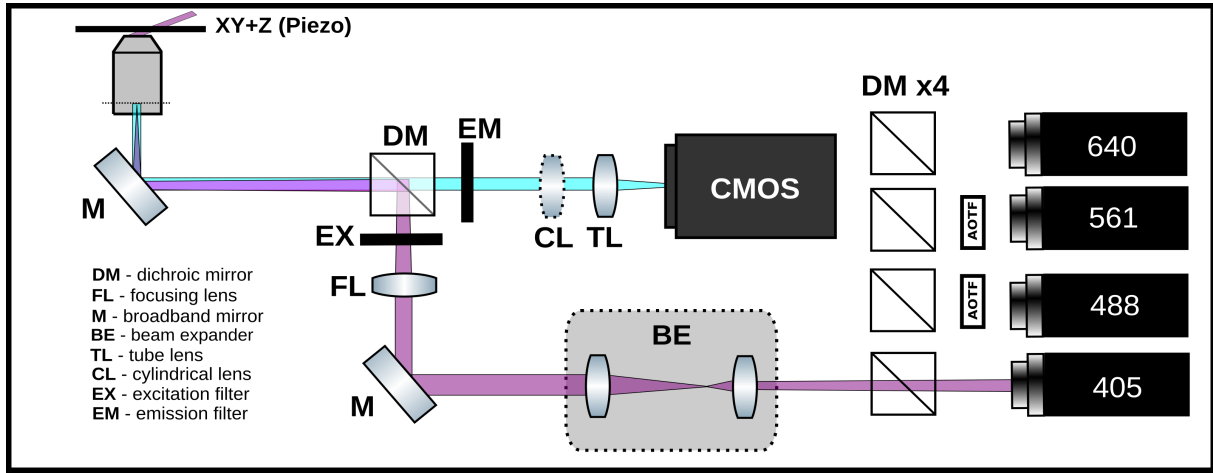


Figure 8: Fluorescence microscopy setup for super-resolution and three-dimensional single molecule tracking. (A) Laser engine and two-path optical relay for selectable EPI with beam expansion (widefield) or HILO illumination based around the ASI RAMM modular system (B) Custom Olympus IX83 build with removable cylindrical lens for three-dimensional single molecule tracking or HILO illumination

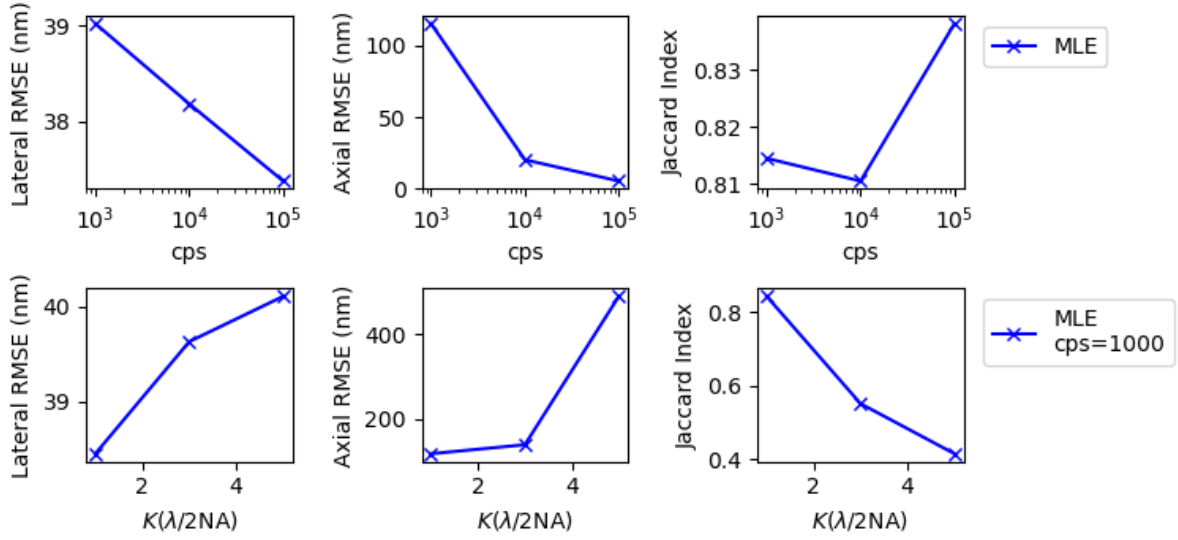


Figure 9: Dependence of axial and lateral precision on SNR and molecular density. (upper row) Lateral and axial root mean squared errors (RMSE) at varying signal levels (lower row) Lateral and axial RMSE for varying molecule counts within a diffraction limit radius for 10^3 photon counts. Error samples = 10^3

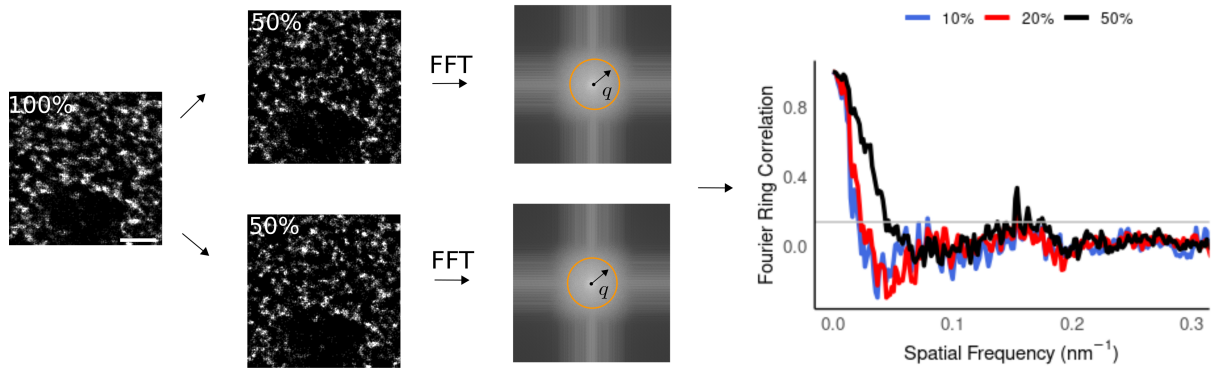


Figure 10: Fourier ring correlation links spatial and temporal resolution. A pair of subsets is drawn from the full list of localizations, and isotropic Gaussian kernel density estimation is performed. The Fourier Ring Correlation is calculated for the pair and plotted as a function of spatial frequency.

described by a Poisson process (Schottky 1918). A shot-noise limited image with N pixels is then described as a family of Poisson variables, with units of photoelectrons

$$\vec{S} = [\text{Poisson}(\mu_1), \text{Poisson}(\mu_2), \dots, \text{Poisson}(\mu_N)] \quad (7)$$

CMOS sensors also suffer from other noise sources, such as readout noise or dark current, resulting in a nonzero signal even in the absence of incident light. Dark current is due to statistical fluctuations in the photoelectron count within a semiconductor material in thermal equilibrium. Fortunately, these additional noise sources are governed by the central limit theorem, and can be efficiently summarized as the component of the noise which exhibits a Gaussian distribution. Readout noise has been often neglected in localization algorithms because its presence in EMCCD cameras is small enough that it can be ignored within the tolerances of the localization precision. In the case of high speed CMOS cameras, however, the readout noise of each pixel is significantly higher and, in addition, every pixel has its own noise and gain characteristic sometimes with dramatic pixel-to-pixel variations (Huang 2013). Therefore, accurate localization and simulation necessitates models which incorporate detailed sensor properties.

0.5.2 Integrated isotropic and anisotropic Gaussian point spread functions

For the sake of simplicity, it is common to describe the point spread function (PSF) as a two-dimensional isotropic Gaussian (Zhang 2007). This is an approximation to the more rigorous models given by Richards and Wolf (1959) or Gibson and Lanni (1989).

$$G(x, y) = \frac{1}{2\pi\sigma^2} e^{-\frac{(x-x_0)^2+(y-y_0)^2}{2\sigma^2}}$$

The characteristic width σ of the PSF typically depends on the numerical aperture of the objective lens and The image of a fluorescent molecule captured by the objective lens, can

be thought of as two-dimensional histogram of photon arrivals and a discretized form of the classical intensity profile $G(x, y)$. The value at a pixel approaches an integral of this density over the pixel:

$$\mu_k = i_0 \lambda_k = i_0 \int_{\text{pixel}} G(x, y) dx dy \quad (8)$$

Let (x_k, y_k) be the center of pixel k . If a fluorescent molecule is located at (x_0, y_0) , the probability of a photon arriving at pixel k per unit time reads

$$\lambda_k = \int_{x_k - \frac{1}{2}}^{x_k + \frac{1}{2}} G(x - x_0) dx \int_{y_k - \frac{1}{2}}^{y_k + \frac{1}{2}} G(y - y_0) dy$$

where $i_0 = g_k \eta N_0 \Delta$. The parameter η is the quantum efficiency and Δ is the exposure time. N_0 represents the number of photons emitted per unit time. We can then express the Gaussian integrals over a pixel by making use of the error function, giving a convenient expression for the fraction of photons which arrive at a pixel k

$$\lambda_k = \frac{1}{4} \left(\operatorname{erf} \left(\frac{x_k + \frac{1}{2} - x_0}{\sqrt{2}\sigma} \right) - \operatorname{erf} \left(\frac{x_k - \frac{1}{2} - x_0}{\sqrt{2}\sigma} \right) \right) \left(\operatorname{erf} \left(\frac{y_k + \frac{1}{2} - y_0}{\sqrt{2}\sigma} \right) - \operatorname{erf} \left(\frac{y_k - \frac{1}{2} - y_0}{\sqrt{2}\sigma} \right) \right)$$

It is also straightforward to generalize this result when G is an anisotropic Gaussian, by replacing σ with either σ_x or σ_y .

0.6 References

- [1] Schermelleh, L. et al. Super-resolution microscopy demystified. *Nature Cell Biology* vol. 21 72–84 (2019).

- [2] Speiser, A. et al. Deep learning enables fast and dense single-molecule localization with high accuracy. *Nat Methods* 18, 1082–1090 (2021).
- [3] Barth, R., Bystricky, K. Shaban, H. A. Coupling chromatin structure and dynamics by live super-resolution imaging. *Sci. Adv* vol. 6 (2020).
- [4] Chen, R. et al. Single-frame deep-learning super-resolution microscopy for intracellular dynamics imaging. *Nat Commun* 14, (2023).
- [5] Dertinger, T., Colyer, R., Iyer, G., Weiss, S. Enderlein, J. Fast, background-free, 3D super-resolution optical fluctuation imaging (SOFI). *PNAS*
- [6] Richards, B. Wolf, E. Electromagnetic Diffraction in Optical Systems. II. Structure of the Image Field in an Aplanatic System. Source: *Proceedings of the Royal Society of London. Series A, Mathematical and Physical Sciences* vol. 253 (1959).
- [7] Devaiah, B. N. et al. BRD4 is a histone acetyltransferase that evicts nucleosomes from chromatin. *Nat Struct Mol Biol* 23, 540–548 (2016).
- [8] Ouyang, W., Aristov, A., Lelek, M., Hao, X. Zimmer, C. Deep learning massively accelerates super-resolution localization microscopy. *Nat Biotechnol* 36, 460–468 (2018).
- [9] Filippakopoulos, P. et al. Selective inhibition of BET bromodomains. *Nature* 468, 1067–1073 (2010).
- [10] Chao, J., Sally Ward, E. Ober, R. J. Fisher information theory for parameter estimation in single molecule microscopy: tutorial. *Journal of the Optical Society of America A* 33, B36 (2016).
- [10] Grimm, J. B. et al. A General Method to Improve Fluorophores Using Deuterated Auxochromes. *JACS Au* 1, 690–696 (2021).
- [12] Nehme, E. et al. DeepSTORM3D: dense 3D localization microscopy and PSF design by deep learning. *Nat Methods* 17, 734–740 (2020).
- [13] Itoh, Y. et al. 1,6-hexanediol rapidly immobilizes and condenses chromatin in living human cells. *Life Sci Alliance* 4, (2021).

- [14] Han, X. et al. Roles of the BRD4 short isoform in phase separation and active gene transcription. *Nat Struct Mol Biol* 27, 333–341 (2020).
- [15] Tokunaga, M., Imamoto, N. Sakata-Sogawa, K. Highly inclined thin illumination enables clear single-molecule imaging in cells. *Nat Methods* 5, (2007).
- [16] Kalisvaart, D. et al. Precision in iterative modulation enhanced single-molecule localization microscopy. *Biophys J* 121, 2279–2289 (2022).
- [17] Zhang, B., Zerubia, J. Olivo-Marin, J.-C. Gaussian approximations of fluorescence microscope point-spread function models. (2007).
- [18] Los, G. V. et al. HaloTag: A novel protein labeling technology for cell imaging and protein analysis. *ACS Chem Biol* 3, 373–382 (2008).
- [19] Bannister, A. J. Kouzarides, T. Regulation of chromatin by histone modifications. *Cell Research* vol. 21 381–395 (2011).
- [20] Singh, R., Ghosh, D. Adhikari, R. Fast Bayesian inference of the multivariate Ornstein-Uhlenbeck process. *Phys Rev E* 98, (2018).
- [21] Holtzer, L., Meckel, T. Schmidt, T. Nanometric three-dimensional tracking of individual quantum dots in cells. *Appl Phys Lett* 90, (2007).
- [22] Ricci, M. A., Manzo, C., García-Parajo, M. F., Lakadamyali, M. Cosma, M. P. Chromatin fibers are formed by heterogeneous groups of nucleosomes in vivo. *Cell* 160, 1145–1158 (2015).
- [23] Hogg, S. J. et al. BET-Bromodomain Inhibitors Engage the Host Immune System and Regulate Expression of the Immune Checkpoint Ligand PD-L1. *Cell Rep* 18, 2162–2174 (2017).
- [24] Smith, C. S., Joseph, N., Rieger, B. Lidke, K. A. Fast, single-molecule localization that achieves theoretically minimum uncertainty. *Nat Methods* 7, 373–375 (2010).
- [25] Sabari, B. R. et al. Coactivator condensation at super-enhancers links phase separation and gene control. *Science* (1979) 361, (2018).

- [26] Linde, S. Van De et al. Direct stochastic optical reconstruction microscopy with standard fluorescent probes. *Nat Protoc* 6, 991–1009 (2011).
- [27] Huang, F. et al. Video-rate nanoscopy using sCMOS camera-specific single-molecule localization algorithms. *Nat Methods* 10, 653–658 (2013).
- [28] Ashwin, S. S., Nozaki, T., Maeshima, K. Sasai, M. Organization of fast and slow chromatin revealed by single-nucleosome dynamics. *Proc Natl Acad Sci U S A* 116, 19939–19944 (2019).
- [29] Hnisz, D., Shrinivas, K., Young, R. A., Chakraborty, A. K. Sharp, P. A. A Phase Separation Model for Transcriptional Control. *Cell* vol. 169 13–23 (2017).
- [30] Grimm, J. B. et al. A general method to improve fluorophores for live-cell and single-molecule microscopy. *Nat Methods* 12, 244–250 (2015).
- [31] Nozaki, T. et al. Dynamic Organization of Chromatin Domains Revealed by Super-Resolution Live-Cell Imaging. *Mol Cell* 67, 282-293.e7 (2017).
- [32] Xu, J. et al. Super-Resolution Imaging of Higher-Order Chromatin Structures at Different Epigenomic States in Single Mammalian Cells. *Cell Rep* 24, 873–882 (2018).
- [33] Boettiger, A. N. et al. Super-resolution imaging reveals distinct chromatin folding for different epigenetic states. *Nature* 529, 418–422 (2016).
- [34] Nozaki, T. et al. Dynamic Organization of Chromatin Domains Revealed by Super-Resolution Live-Cell Imaging. *Mol Cell* 67, 282-293.e7 (2017). [35] Nieuwenhuizen, R et al. Measuring image resolution in optical nanoscopy. *Nature Methods* 10. 557-562 (2013).